Abstract

A multi-purpose platform is an offshore system designed to serve the purposes of more than one offshore industry. Within the context of “The Blue Growth Farm” project, an innovative multi-purpose configuration, comprising a wind turbine, wave energy converters, and an internal pool to accommodate aquaculture fish cages, has been proposed. The present work proposes a framework to assess the coupled dynamic response of the multi-purpose platform in realistic environmental conditions. A simplified parametric analysis of the structure is first carried out to propose a preliminary design of the platform. The preliminary design is subsequently investigated through hydro-elastic and aero-hydro-servo-elastic coupled analyses. Modal analysis is performed through a 3D finite-element structural model. It confirms the feasibility of rigid-body hypothesis for the dynamic analysis of the support structure and manifests that the vibration modes of the structure are not excited by wave or wind loads. In order to assess the coupled dynamic responses, an aero-hydro-servo-elastic coupled numerical model is developed. The motion and structural responses in operational and survival states are investigated. A modified mean up-crossing rate method has been employed to assess the ultimate limit state. The results obtained from the present research confirm the technical feasibility of the proposed configuration and provide a reference for further studies on similar concepts.

Keywords: multi-purpose platform; floating wind turbine; wave energy converter; parametric analysis; hydro-elastic analysis; coupled dynamic analysis; ultimate limit state

1 Introduction

1.1 Context

In its communication entitled “*Blue Growth - opportunities for marine and maritime sustainable growth*” (European Commission, 2012), the European Union (EU) formally acknowledged three important factors: rapid progress is being made in the development of offshore technologies, including those targeting deep waters, the finite nature of land and freshwater resources, which are at an increased strain as a result of economic

development, and the opportunity offered by offshore renewable energy resources to reduce the anthropogenic greenhouse gas emissions, which has been identified as the major cause of climate change (Pachauri et al., 2014).

The “Blue Economy” already accounted for 5.4 million jobs across the EU way back in 2011. It was generating a gross added value of 500 billion euro every year, with huge potential for innovation and growth (European Commission, 2011; European Commission, 2018). Therefore, a number of research initiatives were funded, furthering the knowledge and understanding in this field to find sustainable, techno-economically feasible solutions.

Among these, there have been a number of projects proposing, as a technological solution for the blue growth economy, multi-purpose platforms (H2Ocean, 2012; MERMAID, 2014; Tropos, 2012). A multi-purpose platform (MPP) can be defined as an offshore system designed to serve the purposes of more than one offshore industry.

It is within this context that the project “The Blue Growth Farm” (BGF) (Blue Growth Farm, 2019; Lagasco et al., 2019) has been funded, aimed at performing a techno-economic-socio-environmental assessment of an MPP consisting of a large wind turbine, a series of wave energy converters (WECs), supported by a platform with an internal pool used for a number of aquaculture fish cages. In the present work, the framework developed to support the design of this novel platform for the Blue Economy is presented, focusing on the technological aspects and, in particular, on assessing and enhancing the dynamic response of the system to the environmental loads.

1.2 Previous work and problem statement

Since the MPP is an emerging offshore floating structure concept, the available guidelines and standards issued by the classification and certification authorities are not directly applicable. Some studies on the combined use of multiple ocean resources have been conducted and reported by previous researchers. Aubault et al. (2011) incorporated an oscillating-water-column type WEC into a semi-submersible floating wind turbine. In their work, the theory of such modelling was summarised. It was shown that the overall economic cost could be reduced by sharing mooring and power infrastructure. Muliawan et al. (2013) studied the dynamic response and the power performance of a combined

SPAR-type floating wind turbine and coaxial floating wave energy converter in operational conditions. The analysis was performed in several operational conditions and the simulation results indicated that a synergy between wind and wave energy generation was achieved. Li et al. (2018c) further extended this hybrid offshore renewable energy system and investigated its structural responses (Li et al., 2018a; Li et al., 2019b). Michailides et al. (2014) incorporated a flap-type WEC to a semi-submersible floating wind turbine and investigated the effect of WECs on the response of the integrated system. Their study showed that the combined operation of the rotating flaps resulted in an increase of the produced power without affecting the critical response quantities of the semi-submersible platform significantly. Bachynski and Moan (2013) studied the effects of 3 point absorber WECs on a TLP floating wind turbine in operational and 50-year extreme environmental conditions, in terms of power take-off, structural loads and platform motions. According to their research, reduced surge and pitch motions were observed in operational conditions, while increased pitch motions and tendon tension variations were observed in extreme conditions.

MPP concepts are not limited to renewable energy production but can generally include other facilities aimed to aquaculture, desalinisation, military activities, recreation and residential areas, etc. (Dalton et al., 2019; Bard, 2014; Lamas-Pardo et al., 2015). As the number and size of a MPP sub-systems increase, the platform itself grows in size, up to the order of hundreds or thousands of meters per side. The development of such large (LFS) or very large (VLFS) floating structures still requires a significant amount of research, as a number of new challenges with respect to traditional floating structures arises (Wang and Tay, 2011), particularly due to the modelling of the coupled dynamic model of each sub-system and structure elasticity. An up-to-date review of numerical approach strategies currently available for the hydro-elastic analysis of VLFS can be found in (Wei et al., 2018), where a time-domain hydro-elasticity method able to take into account inhomogeneity of waves in coastal areas is also proposed.

When dealing with an innovative MPP concept, i.e., the floating platform of the present study, it is then crucial to take into account multiple issues, including proper dynamic

coupling of the different sub-systems and potential hydro-elastic effects, due to the relatively large size of the platform.

1.3 Aim

The primary objective of the present research is to propose a preliminary design of a novel MPP concept, within the context of the BGF project, and assess its technical feasibility. The assessment consists in three main steps: (1) to check whether the resonant platform global motions will be excited by linear wave force frequencies through parametric analysis; (2) to check whether the structural vibration mode of the platform will be excited by external loads or not, exploring the necessity to include the elasticity of the platform in the coupled model of dynamics; (3) to estimate the coupled dynamic response and ultimate limit state of the integrated system under joint wind-wave excitations.

The present work therefore proposes a three-levels approach, specific for multi-purpose platforms, to analyse the complex dynamics of these novel offshore structures, and to support their design.The approach proposed is flexible enough to be able to quickly analyse a range of platforms, yet accurate enough to derive the main design decisions. It is hence suitable to support a conceptual/preliminary design of the overall platform. The results obtained prove the feasibility of the innovative MPP concept and of the analysis framework provided. This could be regarded as a useful contribution to the state-of-art research about MPP concepts.

2 Material and methods

The structure concept introduced within BGF project is a concrete rectangular-shaped semi-submersible platform, as schematically shown in Figure 1. The DTU 10MW reference wind turbine (Bak et al., 2013) is adopted as wind energy conversion, while the REWEC3 OWC concept (Boccotti, 2002) is adopted for wave energy conversion. The wind turbine is installed in the forward side, as well as the WECs. The latter are accommodated in the concrete breakwater, protecting the internal pool, where the fish cages for aquaculture are housed. Some openings are present in the aft side, to facilitate

water exchange. The structure shape enables modular construction of each side, thus reducing costs.

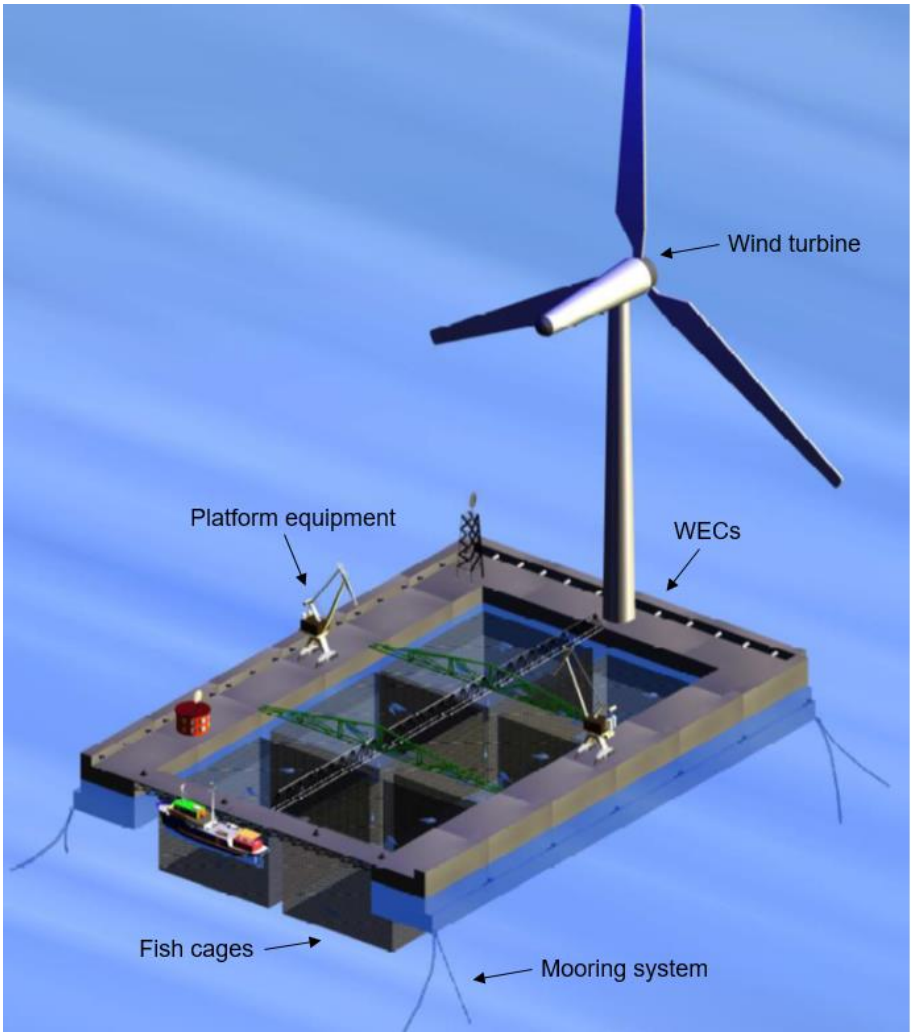

Figure 1: Schematic view of the platform concept

The analysis methodology proposed in this work is organised in three stages. The overall analysis procedure is presented in Figure 2. First of all, a quick but flexible parametric analysis of the concrete platform cross section is carried out (Section 2.1). It is aimed to establish an optimised geometric configuration, whose rigid body heave, pitch and roll natural periods are outside the frequency range of the first-order wave loads. Such a basilar step is necessary due to the innovative nature of the platform and provides a basis for the following analyses as well for future studies on similar platform concepts.

Secondly, the hydro-elastic behaviour of the platform is investigated by means of a full three-dimensional structural modal analysis (Section 2.2) in Ansys, aimed to estimate the role played by the flexible modes among the overall platform dynamics. Indeed, the common literature hypothesis of rigid body dynamics needs to be carefully considered and justified, because of the relatively large dimensions of the innovative platform concept proposed.

Based on the results of the first two steps, the frequency- and time-domain analyses of the final configuration are carried out, regarding the concrete platform as a rigid body. A code-to-code validation between two different potential theory solvers (Ansys AQWA and Wadam) in the frequency domain is performed, due to the complexity of the structure geometry and to the absence of reference results in literature for similar platform concepts. Finally, a time-domain aero-hydro-servo-elastic coupled model is developed in SIMO/RIFLEX, which is used to simulate the dynamic response of the multi-purpose platform (Section 2.3). Based on the simulated dynamic response, the ultimate limit state is assessed using a modified up-crossing rate method. The model has several simplifications and limitations, particularly concerning the WEC representation as a linear damping force, however it provides a very useful framework for the primary assessment of structure dynamic characteristics and feasibility and for future, and more detailed analyses.

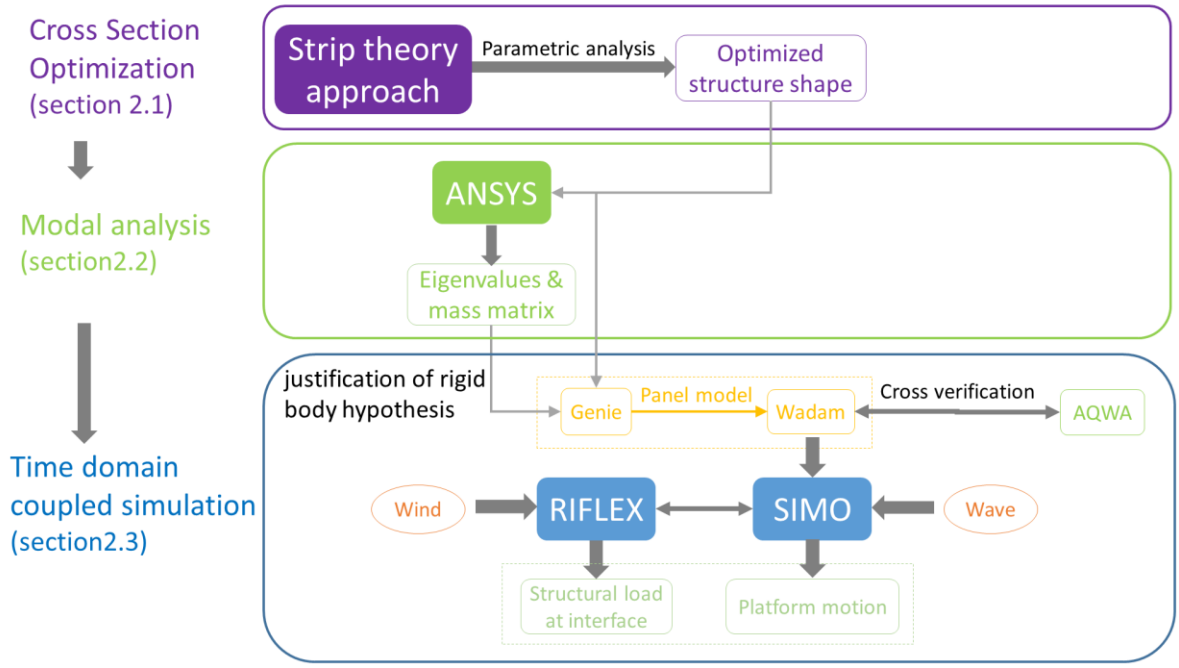

Figure 2 Methodology flow chart

2.1 Caisson transversal section parametric analysis

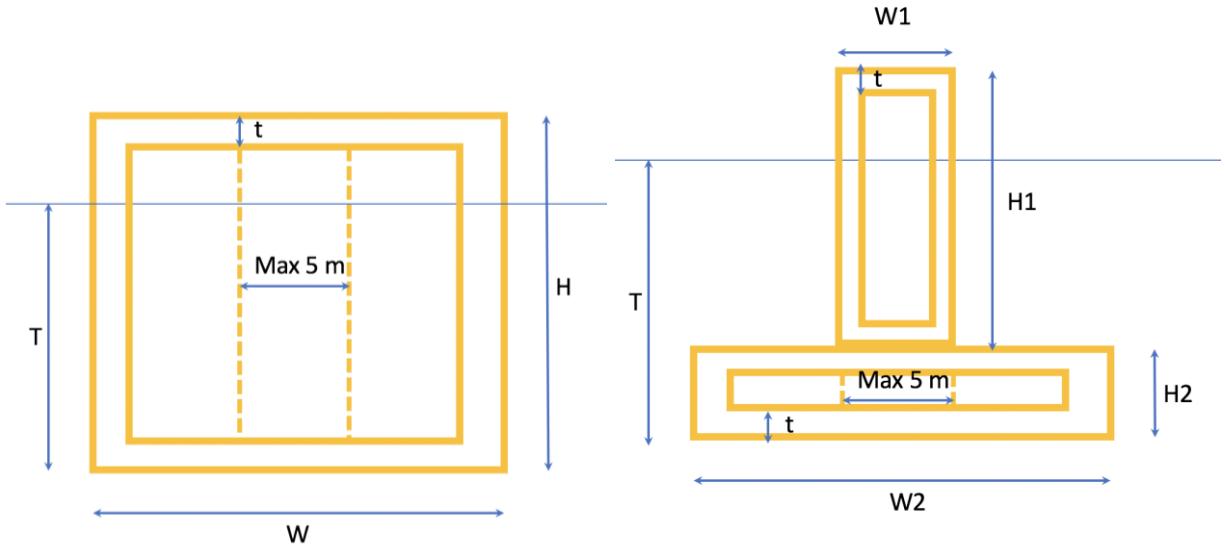

Figure 3 Caisson square (left) and 'Inverse T' (right) cross section. T = draft, H = overall height or H_1 and H_2 = upper and lower caisson heights, W = overall width or W_1, W_2 = upper and lower caisson width, t = concrete outer panel thickness. Dashed line represents the internal concrete bulkheads.

The establishment of an optimised cross section for the innovative concrete platform concept proposed is very important to provide a reference shape, not only to be used in the present study, but also for future applications of any similar platform concept. This task has been carried out through a highly simplified and time-efficient first-stage analysis, as described in the following.

The initial caisson cross configuration, only based on basic static analyses, consisted of a square section (see Figure 3). To avoid an excessive dynamic response to waves, due to having rigid-body motion natural periods within the first order wave load period range (typically between 5 and 25 seconds) (Bachynski, 2018), a simplified 1-DOF approach has been adopted, deriving an approximate but simple and robust expression, allowing the quick estimation of the natural period in heave.

It can be demonstrated that, for this section, the natural period in heave, $T_{33,}$ is:

$$T_{33} = 2\pi\sqrt{\frac{A_{33}+M}{C_{33}}} = 2\pi\sqrt{\frac{\rho C_A A_R L + \rho WTL}{\rho gWL}} = 2\pi\sqrt{\frac{1}{g}\left(C_A\frac{\pi W}{4}+T\right)} \quad (1)$$

where C_A is the added mass coefficient (strip-theory approach, C_A depends on the ratio between T and W (DNV GL, 2017)), A_R the reference area considered for C_A, and L is the length of each caisson (all the same). Using Eq. 1, it is possible to demonstrate that even varying the values of W and T over a wide range, a T_{33} higher than 20-25s (i.e. beyond first order wave loads periods) can only be reached for extremely large W, not compatible with manufacturability and costs limits. The fundamental drawback of the square section is that both the added mass and the hydrostatic stiffness are strongly linked to W, preventing an effective tuning of T_{33}. In order to decouple the two effects, an *'Inverse T'* section has been proposed, as in Figure 3b.

Adopting the same approach as before, for the 'Inverse T' configuration the following can be derived:

$$T_{33} = 2\pi\sqrt{\frac{\pi C_A W_2^2 + H_2 W_2}{W_1 g}} \quad (2)$$

Now, augmenting W_2 only augments the numerator, and therefore T_{33}, without augmenting the denominator (linked to the hydrostatic stiffness), effectively decoupling the added mass from the hydrostatic stiffness. In Table 1 and in Figure 4 are shown the results of the parametric analysis: now the requirement of a T_{33} higher than 20s is fulfilled and an optimized cross section is chosen. Although Eq. 2 is affected by the simplifications assumed in this section (strip theory, 1-DOF, etc.), the pre-design has been successfully verified through more accurate further analysis stages, as detailed in the following sections.

Based on the preliminary parametric analysis conduced, it can be hence concluded that the "inverse-T" cross section represents a good compromise between hydrostatic stiffness and added mass issues of the innovative platform concept proposed. This provides also an indication for future analyses on similar concrete platform concepts.

Table 1: Main cross section design parameters - range of values investigated

Design parameter	Min value (m)	Max value (m)	Final value (m)
Upper caisson width (W1)	4	5	5
Lower caisson width (W2)	24	28	26
Lower caisson height (H2)	6	9	9
Draft (T)	10	25	20
N.B. H1 varied in order to keep the freeboard fixed at 4m			

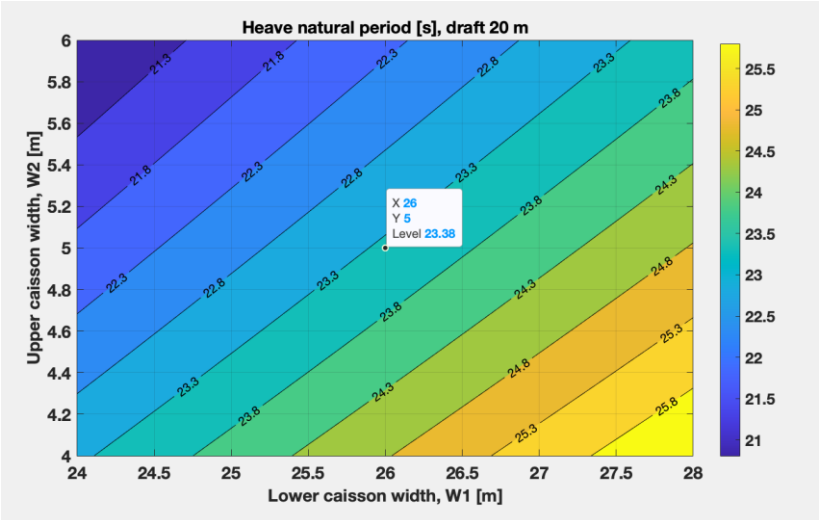

Figure 4: estimated MPP heave natural period, T_{33} (s) – 'Inverse T' cross section. Parametric analysis in function of the upper (W_1) and lower caisson width (W_2). H_2 is 9m, draft 20m, freeboard 4m.

2.2 Hydro-elastic analysis, with flexible platform

The hydro-elastic analysis is aimed to investigate the importance of flexible modes among the overall dynamics of the platform. The hypothesis of structural rigidity, commonly adopted for traditional floating structures, is indeed questioned by the relatively big dimensions of the platform. According to the rule-of-thumb proposed by Lamas-Pardo et al. (Lamas-Pardo et al., 2015), a floating platform should be regarded as a VLFS, and hence treated as an elastic body, when its side length exceeds 10^3 m. This is not the case of the present study, however the platform can be regarded as a LFS and the influence of structure elasticity is uncertain. 3D modal analysis of the structure is hence carried out using the commercial software ANSYS ® (ANSYS, 2020). This approach was proposed by Ruzzo et al. (2019) and adopted by Li et al. (2019a), who showed also its better accuracy and capability of describing torsional modes of the structure, with respect to a simpler 2D beam model of the same structure.

The structure is represented by a set of solid bodies, so as to take into account the detailed internal partition of each caisson, which has resulted from a preliminary structural design. It is relevant to note that the 3D model allows to take into account both longitudinal and transverse internal stiffeners of the caissons, while a 2D representation can include only the former.

Within this structural model, the wind turbine is represented by a simple mass point, i.e. a lumped mass, including also the mass moments of inertia with respect to the three axes. The mass point is placed at the centre of gravity of the wind turbine, and it is rigidly connected to the main structure by a massless constraint. While this representation does not allow to model the flexible dynamic behaviour of the wind turbine, it is compatible with the aim of the modal analysis, which is referred to the support structure only, regarding the wind turbine as an input load. The modes of the wind turbine itself are already well-known from literature (Bak et al., 2013), and should not excite the support structure own natural frequencies.

The wave energy converter internal partition is fully represented from a structural point of view, based on the width of each WEC chamber. The water inside each chamber is

regarded as a mass point, placed at its centre of gravity. This representation allows to properly take into account the mass properties of the WEC. All the other masses, including water ballast and other operational loads (equipment, storage, etc.), are regarded as additional mass points, each placed at its own centre of gravity.

The hydrostatic stiffness in heave, roll and pitch has been represented by a uniform elastic support, applied all over the surface-piercing structural elements, including WECs with their own internal partition. This is equivalent to a vertical spring (per unit area), with a constant value equal to the weight per unit volume of the seawater, which is applied to all the surface-piercing structural elements. The mooring stiffness has been instead represented by means of linear springs, whose stiffness is equivalent to that of the real catenary mooring system. The hydrodynamic added mass has been calculated at this stage adopting a strip theory approach (see Section 2.1). In detail, the 2D added mass per unit length has been derived for each section in horizontal and vertical directions, and a directional mass has been applied to each discrete structure element, obtained by multiplying the added mass per unit length by the corresponding element length.

2.3 Aero-Hydro-Servo-Elastic analysis, with rigid platform

Since the BGF multi-purpose platform accommodates various systems, the development of a fully coupled analysis tool able to simulate the hydrodynamic loads on the platform, WEC hydrodynamics, aerodynamic loads on the wind turbine, structural flexibility, controller dynamics, mooring system dynamics is crucial in the present research. The marine software SIMO-RIFLEX developed by DNV GL is used for the coupled analysis. RIFLEX (SINTEF Ocean, 2019a) is a nonlinear finite element solver for assessing the structural response of flexible structures, e.g. blades, turbine tower and mooring lines. An aerodynamic module based on blade element momentum theory is also embedded for the modelling of wind turbines. SIMO (SINTEF Ocean, 2019b) is a time-domain hydrodynamic analysis code, which calculates the wave loads on the structure based on the potential flow theory. At each simulation time step, the platform motion is transferred to RIFLEX, where the aerodynamic module is called to calculate the wind turbine aero dynamic load (thrust force and torque). The aerodynamic load is then transferred back to

SIMO to update the platform motion. In this way, the coupling of aerodynamic load and platform motion is implemented.

According to the eigenvalues analysis presented in Section 4.1, the structural vibration modes are not excited by wave loads or aerodynamic loads so that the rigid body hypothesis is reasonable, and therefore the concrete platform is regarded as a rigid body. Also, a frequency-domain linear model of the support platform has been implemented autonomously in Ansys AQWA (Aqwa, 2020), to achieve a preliminary code-to-code validation, attaining only the potential flow hydrodynamics of the structure (see Figure 2).

2.3.1 Frequency domain hydrodynamic analysis

The first, pre-processing step before the aero-hydro-servo-elastic analysis consists in a frequency-domain analysis to derive the hydrodynamic coefficients necessary for the time-domain simulations. The necessary frequency-domain analyses have been carried out twice, by two independent teams, and with two different numerical software Wadam (DNV, 1994) and Ansys AQWA (Aqwa, 2020), in order to achieve a first code-to-code verification, due to the lack of experimental values that would allow a validation of the numerical approaches. Within both the models, in addition to the hydrodynamic forces, the following aspects are considered. The mooring system is represented as a linear stiffness, equivalent to the linearised stiffness value at the equilibrium position of the structure. The wind turbine is regarded as a lumped mass, placed at its own centre of gravity. The WECs are represented as mass items too, by ideally closing all the chambers and considering the seawater inside as rigidly moving with the structure. The mass properties of the concrete structure descend from the Ansys structural model described in Section 2.2.

The wave-structure interaction is addressed within the framework of potential flow theory, which separates the wave-structure interaction into diffraction and radiation problems. For each of the two numerical models, a panel model of the platform hull is established, using respectively Genie and Ansys' Geometry module. Each panel model is then imported to the corresponding 3D boundary element analysis software, i.e. Wadam (DNV, 1994) and AQWA (Aqwa, 2020), respectively, to conduct the frequency domain hydrodynamic

analysis. The results obtained at this stage are inclusive of added mass $\mu(\omega)$, radiation damping $\lambda(\omega)$ and wave force transfer function $H(\omega)$.

2.3.2 Time domain aero-hydro-servo-elastic coupled analysis.

2.3.2.1 Hydrodynamics

The wave-structure interaction is addressed within the framework of potential flow theory, based on Cummins' impulse response theory (Cummins, 1962)

$$\sum_{j=1}^{6}\left(M_{ij}+m_{ij}\right)\ddot{x}_j(t)=F_i^{ex}(t)-\sum_{j=1}^{6}\int_0^t\kappa_{ij}(t-\tau)\dot{x}_j(\tau)d\tau-B_{ii}\dot{x}_i(t)-\sum_{j=1}^{6}K_{ij}x_j(t),\ i=1,2,..,6 \qquad (3)$$

where M is the mass matrix of the floater and m is the added mass matrix at infinite frequency. x, $\dot{x}$ and $\ddot{x}$ are the displacement, the velocity, and the acceleration vectors. κ is the retardation function, representing the memory effect of the free surface. K is hydrostatic restoring stiffness matrix. F^{ex} is the wave excitation force, including both 1st-order and 2nd-order components.

The 1st-order wave force is given by

$$F_{ex}^{1st}=\sum_{j=1}^{N}H^{1st}(\omega_j)\cdot\xi_j\cdot e^{i(\omega_j t+\varepsilon_j)},\ \xi_j=\sqrt{2S(\omega_j)\Delta\omega} \qquad (4)$$

where S(ω) is the wave spectrum; ε_j is the random phase of wave component j; $\Delta\omega$ is the frequency discretisation; H^{1st} is the linear wave force transfer function.

The 2nd-order wave force is calculated as:

$$\begin{aligned}&F_{ex}^{2nd}(t)=\mathrm{Re}\left\{u^2+v^2\right\}\\&u=\sum_{j=1}^{N}\sqrt{H^{2nd}(\omega_j,\omega_j)}\,\mathrm{Re}\left\{\xi_j e^{i(\omega_j t+\varepsilon_j)}\right\},v=\sum_{j=1}^{N}\sqrt{H^{2nd}(\omega_j,\omega_j)}\,\mathrm{Im}\left\{\xi_j e^{i(\omega_j t+\varepsilon_j)}\right\}\end{aligned} \qquad (5)$$

where H^{2nd} is the quadratic transfer function of the second order wave force.

B is a linear damping coefficient to account for the viscous effect. The linear damping coefficient is set of 5% of the critical damping, namely $B_{ii}=0.05\times2\sqrt{K_{ii}(M_{ii}+m_{ii})}$.

In spite of the two openings at the aft side, the inner pool is basically a moonpool widely seen in offshore oil and gas platforms. Since the potential flow theory overestimates the

resonance of a constrained water volume (Molin et al., 2009), a damping lid is added to the inner pool to suppress the free surface elevation. A damping factor of 0.02, recommended by Wadam for the investigation on moonpool, is adopted in the present simulation.

2.3.2.2 Aerodynamics

The aerodynamic loads acting on the wind turbine rotor are calculated using an extended blade element momentum (BEM) method (Hansen, 2015). This modified BEM method incorporates the Stig Øye dynamic inflow model (Øye, 1991) to account for the aerodynamic unsteadiness. The aerodynamic modelling is further improved with the addition of Glauert correction (Tony Burton et al., 2001), Prandtl factor (SINTEF Ocean, 2019a) and a dynamic stall model (Hansen, 2015).

2.3.2.3 Wind turbine control

The DTU 10MW wind turbine reference control algorithm (Bak et al., 2013) is utilised in the present research. A variable-speed torque strategy and a blade pitch strategy are incorporated into the controller. The two control strategies are designed to work independently, for the most part, in the below-rated and above-rated wind-speed range, respectively. The goal of the variable-speed torque controller is to maximise the power capture below the rated operation point. The goal of the blade-pitch controller is to regulate the generator power above the rated operation point.

2.3.2.4 Structural and mooring line dynamic

The blades and the tower are modelled as nonlinear beam elements, while the mooring lines are represented by nonlinear bar elements. The dynamic equations are solved in the time domain by using the Newmark-b method (SINTEF Ocean, 2019b). Structural damping is also included by applying the global Rayleigh damping for all flexible finite elements.

2.3.2.5 Wave energy converter

Considering the complexity of the oscillating-water-column WEC (Malara et al., 2017), a simplified model is developed to represent the WEC impact on the main platform to enable a trade-off between simulation accuracy and efficiency.

Assuming that the air is incompressible, the mass flow rate of through the self-rectifying turbine (positive for air going outward) is:

$$\dot{m} = -\rho \dot{V} \tag{6}$$

where ρ is the air density and V the volume of air inside the chamber

$$\begin{aligned} V &= V_0 + (\xi - \eta) S_1 \\ \dot{V} &= (\dot{\xi} - \dot{\eta}) S_1 \end{aligned} \tag{7}$$

where V_0 is the volume of air inside the chamber in calm water, and S_1 is the sectional area of the chamber, η is the wave elevation and ξ is the heave motion of the WEC. Then,

$$\dot{m} = -\rho(\dot{\eta} - \dot{\xi}) S_1 \tag{8}$$

The characteristics of the air turbine used to transform the pneumatic energy into mechanical energy (torque) are represented through the following two parameters:

$$\begin{aligned} \Phi &= \frac{\dot{m}}{\rho \Omega R^3} \\ \Psi &= \frac{p}{\rho \Omega^2 R^2} \end{aligned} \tag{9}$$

where p is the pressure difference; Ω is the rotational speed of the turbine shaft; R is the turbine diameter. For the Wells turbine utilised in the BGF project,

$$\Phi \approx K\Psi, K = 0.6803 \tag{10}$$

In this case:

$$p = \frac{\dot{m}\Omega}{KR} \tag{11}$$

The force applied to the air turbine is

$$F_{WEC} = pS_2 = -\frac{\rho(\dot{\eta} - \dot{\xi})S_1 S_2 \Omega}{KR} \tag{12}$$

where S2 is the area of the air turbine rotor.

Frequency-domain analysis in Wadam shows that $\dot{\eta}(\omega) \approx k(\omega)\dot{\xi}(\omega)$, so it is able to remove the free surface elevation

$$\begin{aligned} F_{WEC} &= -B\dot{\xi} \\ D &= \frac{\rho(k-1)S_1 S_2 \Omega}{KR} \end{aligned} \tag{13}$$

In this way, a linear damping coefficient B can be used to represent the force transferred to the platform. Please note that $\dot{\xi}$ = $\dot{x}_3$+$\dot{x}_5$L (L is the distance from WEC to CG of the platform),

$$\begin{aligned} F_{heave} &= -D(\dot{x}_3 + \dot{x}_5 L) \\ F_{pitch} &= -D(\dot{x}_3 + \dot{x}_5 L) \cdot L \end{aligned} \tag{14}$$

So that

$$\begin{aligned} D_{heave-heave} &= \frac{\rho(k-1)S_1 S_2 \Omega}{KR} \\ D_{pitch-heave} &= D_{heave-pitch} = \frac{\rho(k-1)S_1 S_2 \Omega}{KR} L \\ D_{pitch-pitch} &= \frac{\rho(k-1)S_1 S_2 \Omega}{KR} L^2 \end{aligned} \tag{15}$$

2.4 Ultimate limit state

The ultimate limit state is assessed using the modified mean up-crossing rate method proposed by Naess and Gaidai (2009). Assuming that the random number of up-crossing is approximated by the Poisson distribution, the distribution of ultimate response of a random process *y*(*t*) is described as

$$P(y_{\max} \le y) = \exp\left(-\int_0^T v^+(y,t)dt \right) \tag{16}$$

where $v^+(y,t)$ is the up-crossing rate corresponding to level *y*, which denotes the instantaneous frequency of the positive slop crossings of the defined level. In this circumstance, the probability of y_{max} exceeding a defined level *y* is given by

$$P(y_{\max} > y) = 1 - \exp\left(-\hat{v}^+(y)T\right)$$
$$\hat{v}^+(y) = \frac{1}{T}\int_0^T v^+(y,t)dt \tag{17}$$

The mean up-crossing rate $\hat{v}^+(y)$ can be easily obtained from the time series of the signal that is going to be analysed. For example, if there are *k* independent numerical realisations of the random process and let $n_j^+(y,T)$ denote the number of up-crossings in realisation *j*, then the sample-based mean up-crossing rate is given by

$$\hat{v}^+(y) \approx \overline{v}^+(y)$$
$$\overline{v}^+(y) = \frac{1}{kT}\sum_{j=1}^{k} n_j^+(y,T) \tag{18}$$

Eq. (18) is the original mean up-crossing rate approach, which requests a large amount of data samples. To save computation resources, Naess and Gaidai (2009) modified the original up-crossing rate method through the proposal of an extrapolation model

$$\overline{v}^+(y) \approx v_{fit}^+(y)$$
$$v_{fit}^+(y) = q \cdot \exp\left\{-a(y-b)^c\right\}, y \geq y_0 \tag{19}$$

where *q*, *a, b* and *c* are all constant values. y_0 is the lower limit of the sampled data used for the extrapolation. The least square optimisation method is used to get *q*, *a*, *b* and *c* based on 5 independent numerical realisations (*k* = 5). Figure 5 gives an example of the extrapolation of the sample-based up-crossing rate. Hereinafter, the extrapolated up-crossing rate is used to represent the ultimate response.

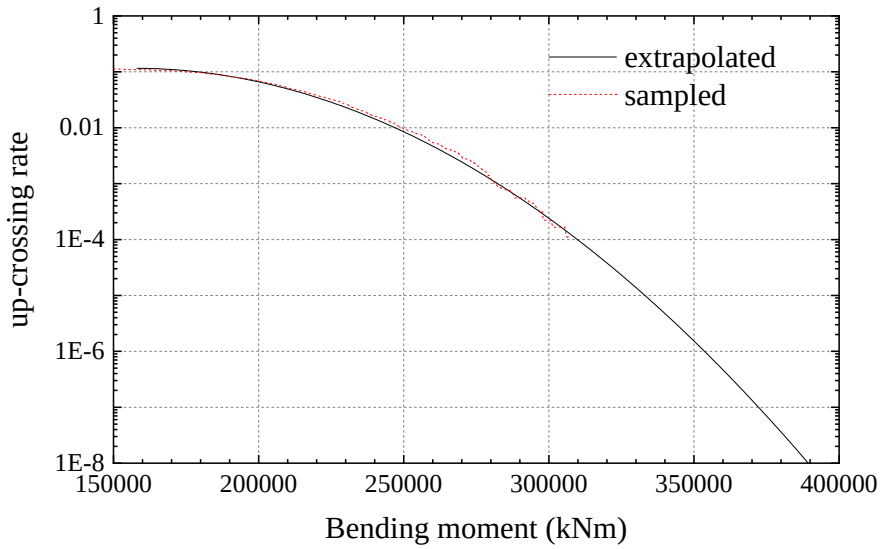

Figure 5 Extrapolation of the sample-based up-crossing rate (LC2, tower base bending moment).

3 Case study

3.1 MPP configuration

The main dimensions of the platform are listed in Table 2. The design water depth is 100m. The platform is moored through 12 catenary chain lines. Figure 6 shows the coordinate system in the present study. The origin *O* is displaced on the still water surface, right at the centre of the inner pool.

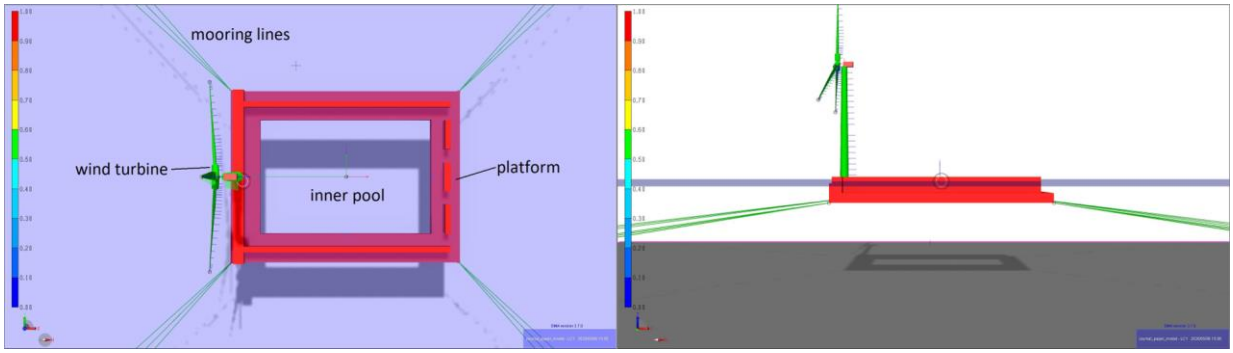

Figure 6 Plan and lateral view of the platform, with indication of the coordinate system used within the present study

Table 2 Main characteristics of the platform

Parameter	Value
Water depth	100 m
Platform size	208 m×156 m
Inner pool size	156 m×104 m
Draft	20 m
Total mass	195,565,613 kg
CoG	(-8.16 m; 0 m; -10.89 m)
Ixx	5.834e+11 kgm^2
Iyy	1.225e+12 kgm^2
Izz	1.738e+12 kgm^2

The DTU 10 WM wind turbine (Bak et al., 2013) is used to harvest power from the offshore wind. The key parameters of the wind turbine including the tower, are given in Table 3.

Table 3 Key parameters of the DTU 10 WM wind turbine

Parameter	Value
Rated wind speed	11.4 m/s
Rated power	10 MW
Rotor diameter	178.3 m
Hub height	119 m
Maximum rotor speed	9.6 rpm
Rotor mass	227,962 kg
Nacelle mass	446,036 kg
Tower mass	628,442 kg

In addition to the wind turbine, the multi-purpose platform also integrates 28 oscillating-water-column WECs. The WECs are based on REWEC3 OWC concept (Boccotti, 2002), as shown in Figure 7, adapted for the application on the floating platform. Each WEC consists of a chamber and a vertical duct. The vertical duct has a size of 2.5 m×5 m, while the chamber has a size of 5 m×5 m. For each WEC, a Wells self-rectifying air turbine is installed to convert the pressure difference within the inner chamber into electricity power. The diameter of the Wells turbine is 1.5m.

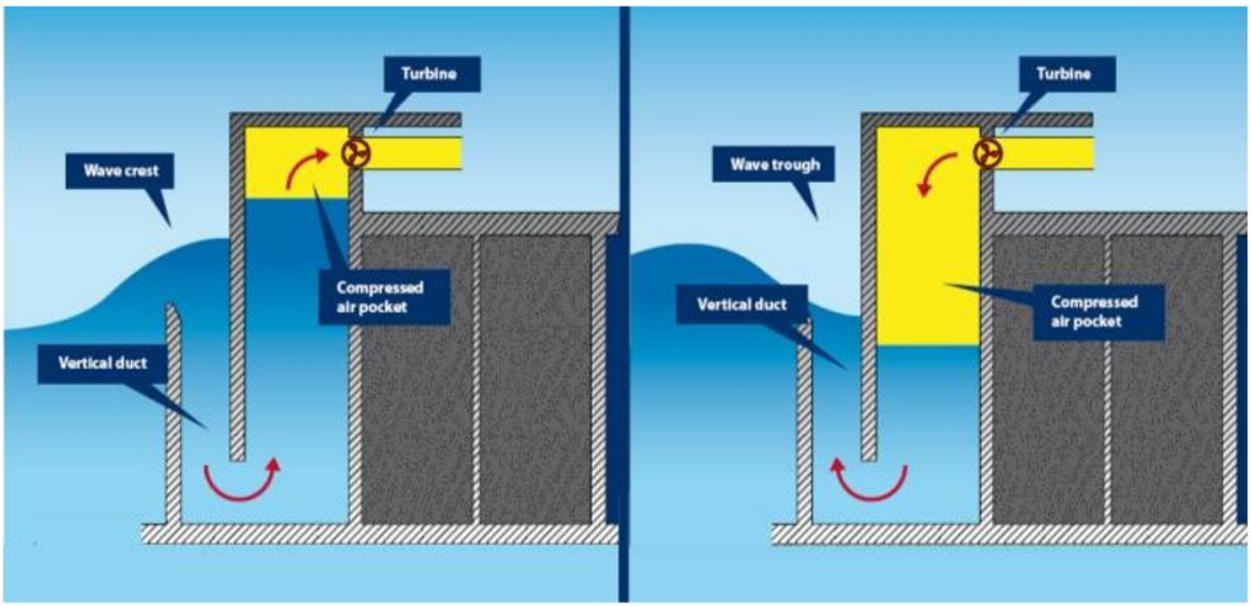

Figure 7 Shape and functioning of the oscillating-water-column WECs installed in the floating platform.

The platform is moored with 12 catenary chain lines. Each 3 lines are connected to one corner of the platform. The mooring line configuration and properties are given in Table 4 and Table 5, respectively. The horizontal restoring stiffness of the mooring system is shown in Figure 8.

Table 4 Configuration of mooring lines

	Fairlead	Anchor
Line1	(104m,78m,-20m)	(705m 621m -100m)
Line2	(104m,78m,-20m)	(675m 652m -100m)
Line3	(104m,78m,-20m)	(644m 682m -100m)
Line4	(104m,-78m,-20m)	(705m -621m -100m)
Line5	(104m,-78m,-20m)	(675m -652m -100m)
Line6	(104m,-78m,-20m)	(644m -682m -100m)
Line7	(-104m,-78m,-20m)	(-705m -621m -100m)
Line8	(-104m,-78m,-20m)	(-675m -652m -100m)
Line9	(-104m,-78m,-20m)	(-644m -682m -100m)
Line10	(-104m,78m,-20m)	(-705m 621m -100m)
Line11	(-104m,78m,-20m)	(-675m 652m -100m)
Line12	(-104m,78m,-20m)	(-644m 682m -100m)

Table 5 Mooring line properties

Parameter	Value
Line length	815 m
Mass per unit length	401 kg/m
Diameter	0.064 m
Axial stiffness	1.7e9 N
Equivalent horizontal mooring stiffness	5.5e6 N/m
Breaking load of each line	1.8e7 N

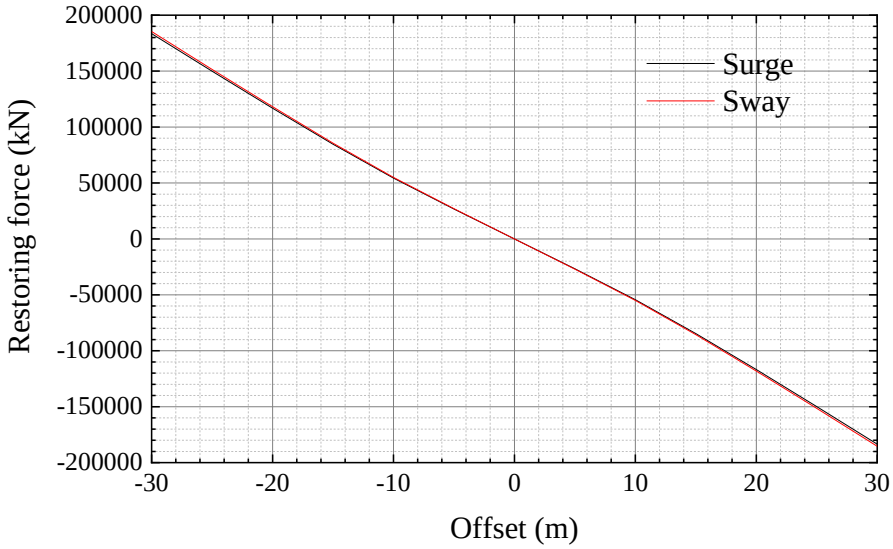

Figure 8 Force-displacement behaviour of the mooring system.

3.2 Requirements and load cases considered

The joint wind-wave environmental conditions are defined based on the joint distribution of wind-wave model proposed by Johannessen et al. (2001)

$$f_{U_{10},H_s,T_p}(u_{10},h_s,t_p) = f_{U_{10}}(u_{10}) \cdot f_{H_s|U_{10}}(h_s\,|u_{10}) \cdot f_{T_p|H_s,U_{10}}(t_p\,|h_s,u_{10}) \tag{20}$$

Eq. (20) is the joint distribution, namely the product of a marginal distribution of wind speed U_{10} at 10 m above the mean surface level, a condition distribution of the significant wave height H_s for given U_{10}, and a condition distribution of wave peak period T_p for given H_s and U_{10}.

In the present research, the Harris spectrum (SINTEF Ocean, 2019b) is used to model the wind turbulence. The wind shear is modelled using the power law

$$u(z) = u_{10}\left(\frac{z}{10}\right)^{0.125} \tag{21}$$

where $u(z)$ is the wind speed at height z. The random ocean waves are modelled with the JONSWAP wave spectrum.

A set of load cases are designed to investigate the coupled dynamics of the multi-purpose platform during various working states: below-rated operation state, rated operation state, above-rated state and survival state. Table 6 lists the load cases considered in the present research. LC4 represents the survival state, in which the wind turbine is parked. For each load, 5 independent 1-hr numerical realisations with different wave and wind seeds are carried out to reduce stochastic variations.

Table 6 Load cases

	u_{hub} (m/s)	u_{10} (m/s)	H_s (m)	T_p (s)
LC1	8	5.86	2.52	9.82
LC2	11.4	8.36	3.09	10.04
LC3	18	13.19	4.36	10.63
LC4	30	22.00	7.11	11.89

4 Results and discussion

4.1 Hydro-elastic analysis, with flexible platform

The 3D structural model developed in ANSYS for the modal analysis is shown in Figure 9. The input data of the structural model descend directly from the structure characteristics described in section 3.1. Hydrodynamic quantities, preliminarily estimated by means of strip theory, and other relevant information are reported in Table 7. Consistency of these data with the following hydrodynamic analyses has been verified.

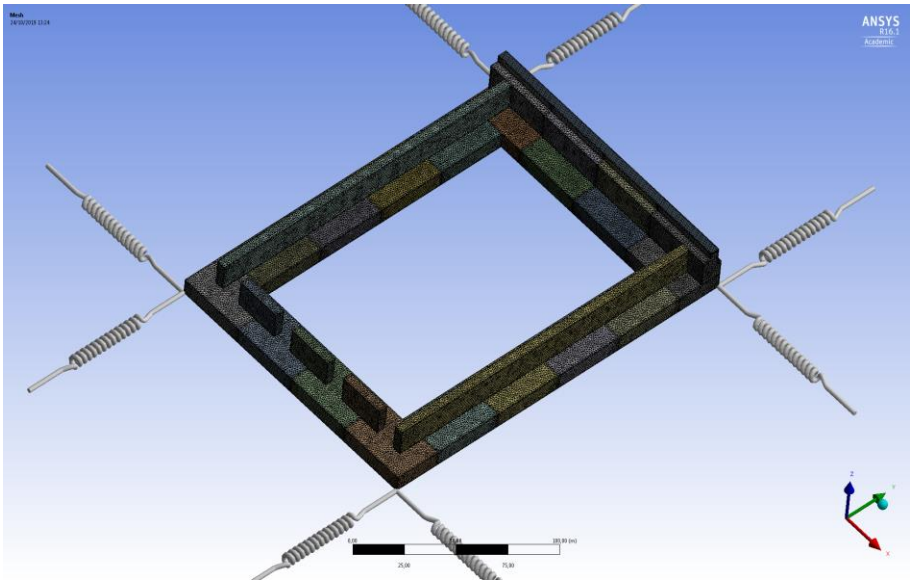

Figure 9: 3D structural model of the platform implemented in ANSYS (with mesh)

Table 7: Main input data of the structural model

Parameter	Value
Young modulus (Pa)	4.0 e10
Total added mass in x-direction (kg)	5.07 e7
Total added mass in y-direction (kg)	6.81 e7
Total added mass in z-direction (kg)	3.15 e8
Total horizontal stiffness in x- and y- directions (N/m)	5.50 e6

The model mesh is made up of about 1.1e6 3D elements, corresponding to a nominal mesh size of 0.6 m. The mesh size value has been set equal to the wall thickness of the caissons, in order to better represent the flexible modes. A sensitivity study has been also carried out to further justify this choice. As an outcome, it has been observed that differences of natural frequency estimations for greater mesh size values are very small. For sake of example, if a mesh size of 2 m is set instead, the number of 3D elements reduces to about 4.4 e5, the natural frequencies of the rigid body motions change by less of 0.5 %, while those of the flexible modes change by less than 4.0 % and also mode shapes and mass participation ratios change accordingly. The sensitivity study hence confirmed the adequacy of the mesh size chosen to the purpose of the present work.

The modal analysis has been carried out for the first eleven modes of the structure. For each of them, mode shape, natural frequency and mass participation ratios for each

direction have been estimated. The results obtained are synthetically listed in Table 8, while the first two flexible mode shapes are shown in Figure 10 as an example.

Table 8: Natural frequencies and mass participation factors estimations

Mode	Natural frequency [rad/s]	Mass participation ratios [%]					
		X	Y	Z	RX	RY	RZ
1	0.144	99.7	2.4 e-5	2.1 e-2	1.4 e-2	0.17	24.5
2	0.149	2.8 e-5	99.4	1.2 e-7	0.19	1.8 e-8	49.2
3	0.218	1.8 e-4	0.27	3.3 e-3	0.20	8.4 e-8	25.9
4	0.222	0.23	6.8 e-5	43.7	28.7	1.18	8.2 e-2
5	0.257	2.3 e-6	0.32	1.1 e-2	34.2	1.3 e-2	0.39
6	0.269	5.6 e-2	2.7 e-5	56.3	36.7	98.6	1.6 e-2
7	1,733	2.0 e-8	6.5 e-6	1.3 e-7	3.6 e-4	2.5 e-8	3.1 e-5
8	3,264	9.4 e-7	7.2 e-9	3.8 e-6	3.1 e-6	3.8 e-6	2.2 e-7
9	4,098	2.4 e-7	2.8 e-9	5.7 e-6	3.7 e.6	2.9 e-6	8.5 e-8
10	4,963	4.0 e-11	2.9 e-8	4.3 e-10	1.4 e-7	8.5 e-10	8.2 e-7
11	6.253	8.4 e-11	1.7 e-8	5.5 e-9	2.7 e-7	4.7 e-8	3.7 e-8

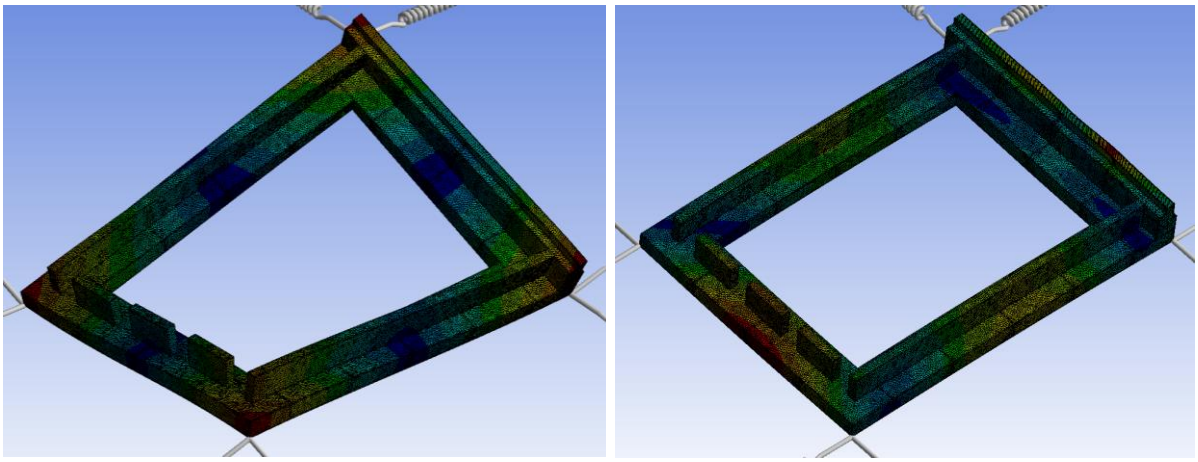

Figure 10: Mode shapes of the first two flexible modes (Left: mode 7; right: mode 8). Red colour indicates the maximum deformation, while blue colour indicates the minimum one.

The most important outcome of the modal analysis is that the first six modes, i.e. those related to the rigid body motions of the structure, cumulatively interest more than 99.99% of the mass in all the directions. In particular, as shown in Table 8, the order of the rigid modes is the following: the first three modes are the pure horizontal motions of surge, sway and yaw, while the other three modes are given by the vertical motions, where heave is coupled with roll and pitch. The mass participation ratios of the following modes, i.e. the first five flexible ones, are substantially negligible (<0.01%). This justifies to carry

out hydrodynamic analyses under the simplifying hypothesis of rigid body. Furthermore, it is relevant to mention that all the natural frequencies fall outside the exciting loads frequencies, as shown in Figure 11. Here, the design loads of interest are represented by the load cases presented in Table 6, in addition to the 1P and 3P wind turbine frequencies (Ruzzo et al., 2019) . Finally, the 3D model allows to consider torsional modes and multi-plane bending characteristics, which could not be captured using a simplified 2D approach. The results obtained provide a detailed insight of structure dynamic properties, thanks to the comprehensive modelling and meshing of the WEC chambers and other structural details.

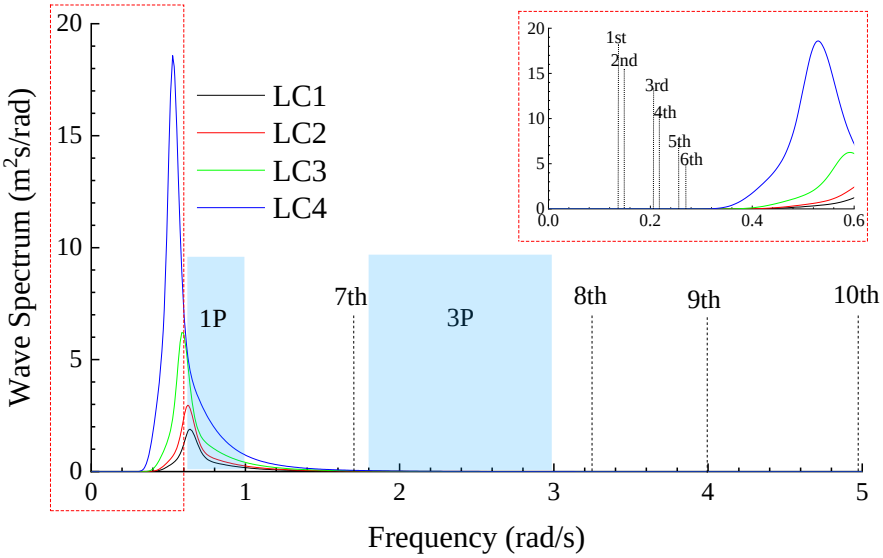

Figure 11 Frequency map: frequencies of oscillation modes compared to the load cases wave spectra and the 1P and 3P range of frequency.

4.2 Aero-Hydro-Servo-Elastic analysis, with rigid platform

4.2.1 Frequency domain

The results of the frequency domain analyses implemented in Wadam and Ansys AQWA are reported and compared in this section, in order to achieve code-to-code validation for the innovative platform concept proposed. Figure 12 to Figure 14 plot the hydrodynamic quantities calculated by the two software, which confirm the overall consistency between the two codes. Negative added masses values and the peaks in added mass and radiation damping plots correspond to the resonant frequencies of the moonpool, which

are clearly identified and consistent with previous literature on moonpools behaviour (Molin et al., 2018, Wolgmamot et al., 2015, Mavrakos, 2004). Minor local differences between the exact results of the two codes are due to the peculiarities of each solver, including mesh discretization. It is worth noting that such minor differences can be deemed negligible in the development of the time-domain aero-hydro-servo-elastic coupled model.

All the hydrodynamics quantities calculated in Wadam (added mass, damping, and wave force transfer function) have been then used in SIMO/RIFLEX, to carry out the time-domain aero-hydro-servo-elastic coupled analysis, as discussed in the next section.

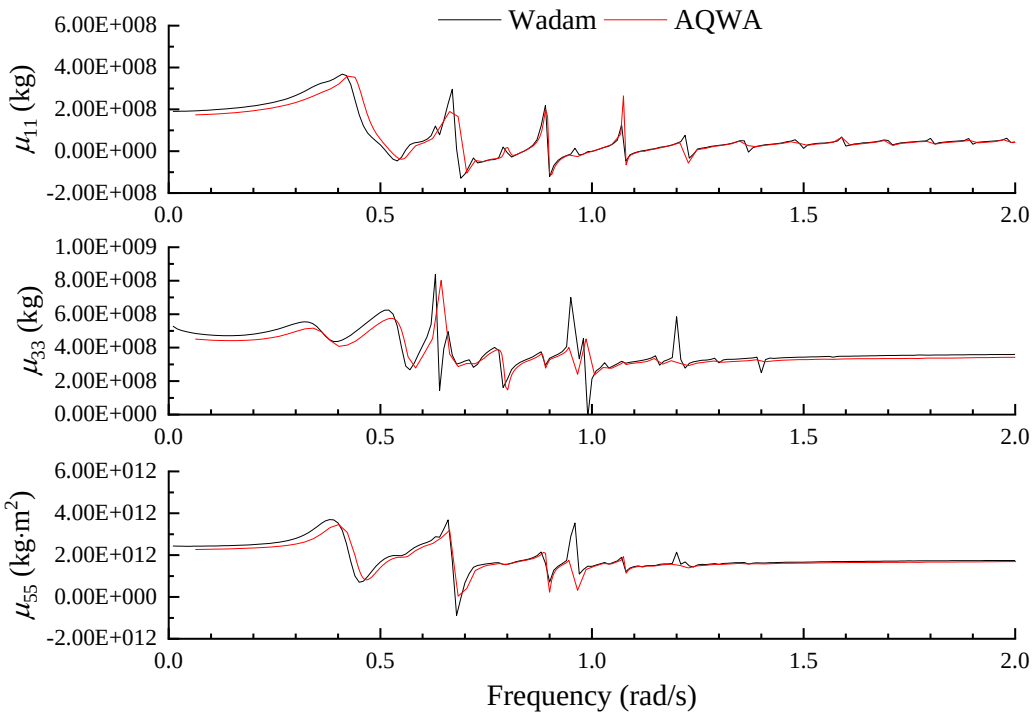

Figure 12 Added mass

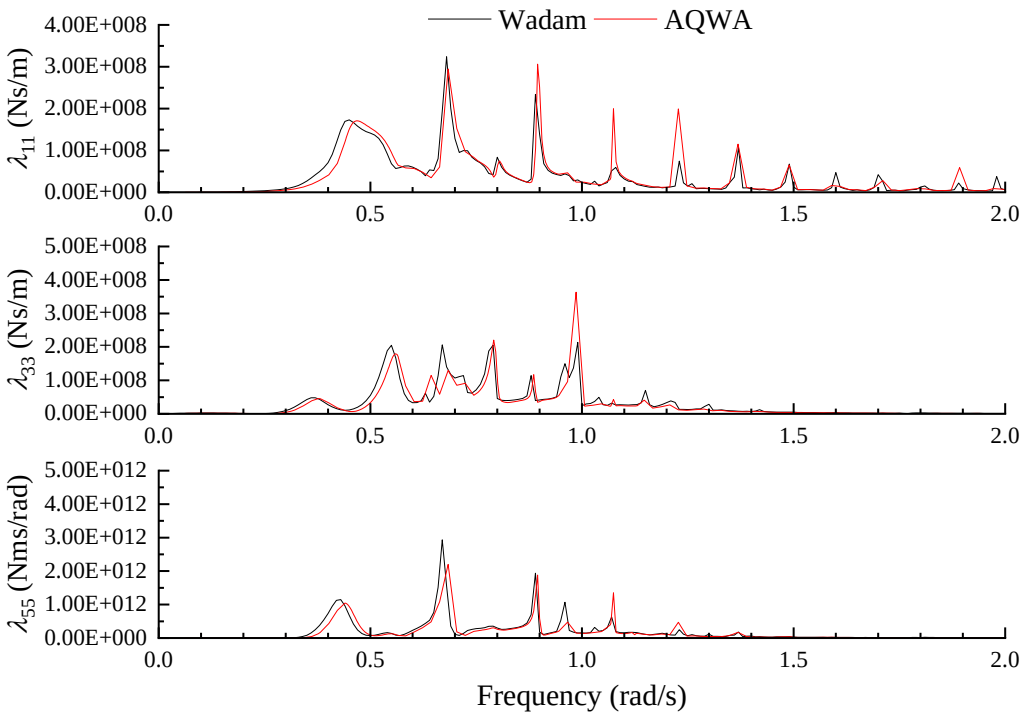

Figure 13 Radiation damping

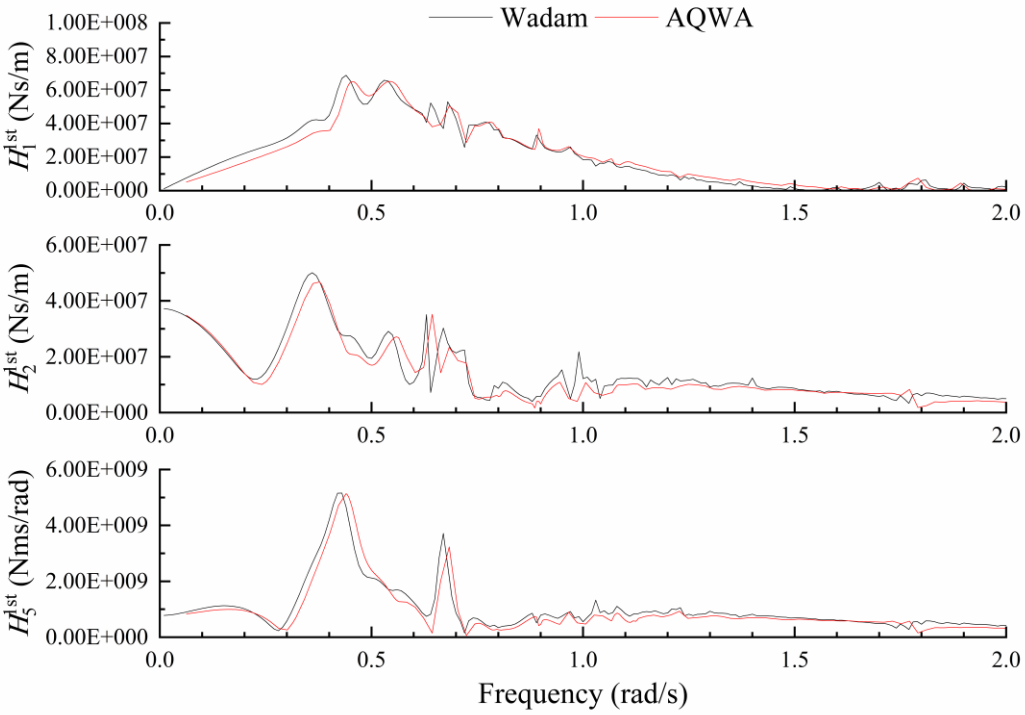

Figure 14 Wave force transfer function

4.2.2 Time domain

The hydrodynamic response of the platform under wave load is investigated in Section 4.2.1, using a frequency domain approach. The coupled dynamic response under the joint action of wave, wind, control and mooring lines is addressed in this section in the time domain, using the coupled numerical model described in Section 2.3.2. All the results presented are based on five independent numerical simulations with different wave seeds.

4.2.2.1 Dynamic motions

The mean value and standard deviation of platform motions are analysed and shown in Figure 15. The platform motions increase with the severity of the ocean waves, as expected. Due to the wind turbine thrust force and mean wave drift force, the mean surge position is non-zero. Although the thrust force also generates a pitch moment, the mean pitch motion is nearly zero due to the huge pitch restoring stiffness. It is interesting to find that the mean surge position is the largest in LC4, even if the wind turbine is parked. It is attributed to the mean drift wave force.

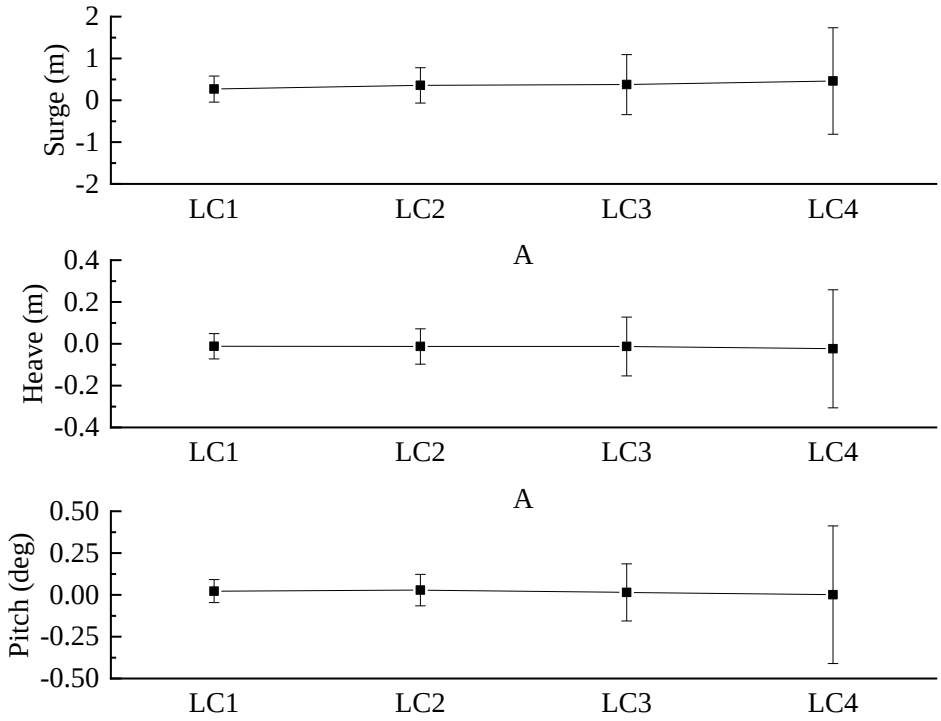

Figure 15 Mean value and standard deviation of platform motions.

To further investigate the coupled dynamic response to external excitation loads, the power spectrum density (PSD) of the platform motions are presented in Figure 16, where a multi-modal response is observed. The platform is primarily excited around the wave-dominated frequency range due to the 1st-order linear wave force. In addition, the surge motion is also stimulated significantly around 0.02 Hz, namely the surge natural period. The surge resonant motion is induced by the 2nd-order wave force, the varying frequency of which is much lower than the first order line wave force. The significance of 2nd-order wave force to the motions of floating semi-submersible structures has been proved by both model test (Li et al., 2018b) and numerical simulation (Coulling et al., 2013). In addition to the resonant response, very low frequency surge motion is also observed, which is induced by the wind turbulence. The turbulence spectrum is mainly dominated by low frequency component so that the wind turbine thrust force varies slowly. Nevertheless, the low frequency surge motion is much smaller than the resonant and wave frequency motions. Heave and pitch resonant motions are observed as well, but of minor importance compared with the wave frequency motions. The effect of aerodynamic load on heave and pitch motions is negligible. It is concluded that the platform motions are dominated by wave loads.

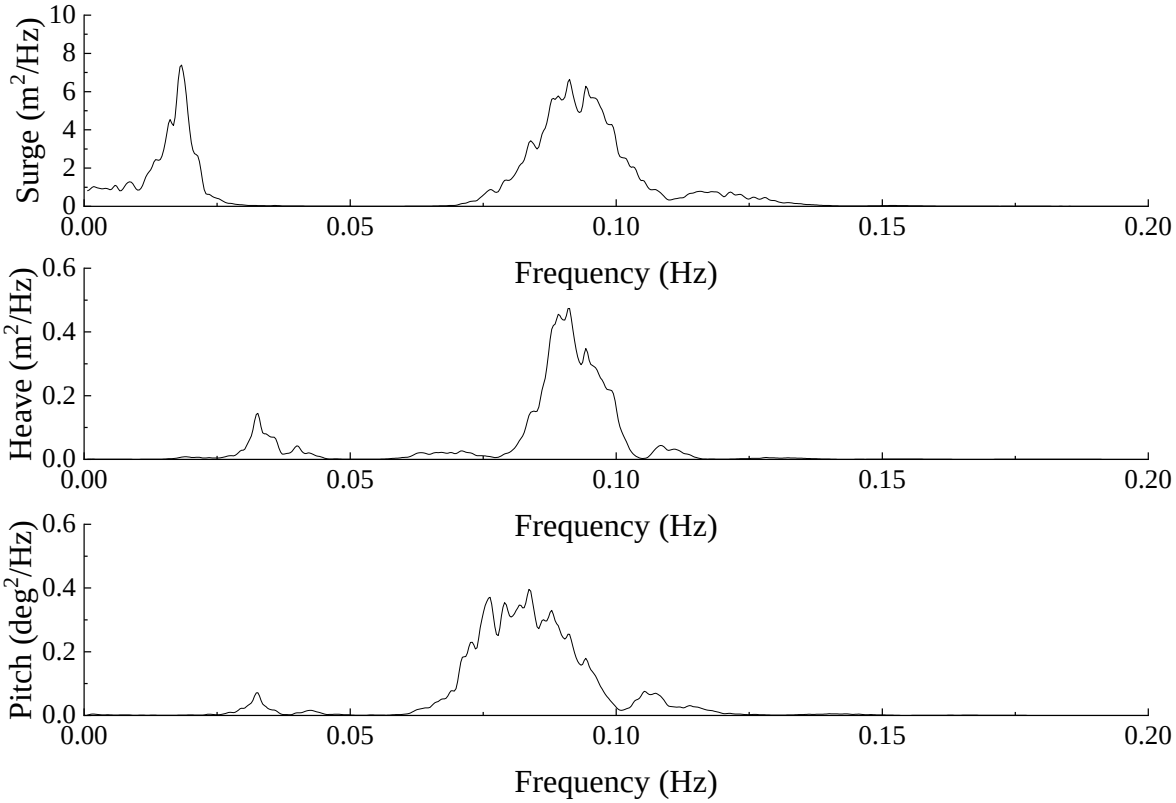

Figure 16 PSD of platform motions, LC2.

Apart from the platform motion, the nacelle motion is another essential index to evaluate the performance of the multi-purpose system as the equipment installed inside the nacelle, while in operational conditions, can be damaged by excessive accelerations. Figure 17 plots the time series of the nacelle surge motion. It is found that the strongest nacelle response occurs in LC4, in which the wave load is the most substantial. Table 9 summaries the maximum nacelle acceleration in the load cases considered in the present research. In the survival state, the nacelle is subject to substantial inertial load, with the maximum acceleration hitting 3.39 m/s^2.

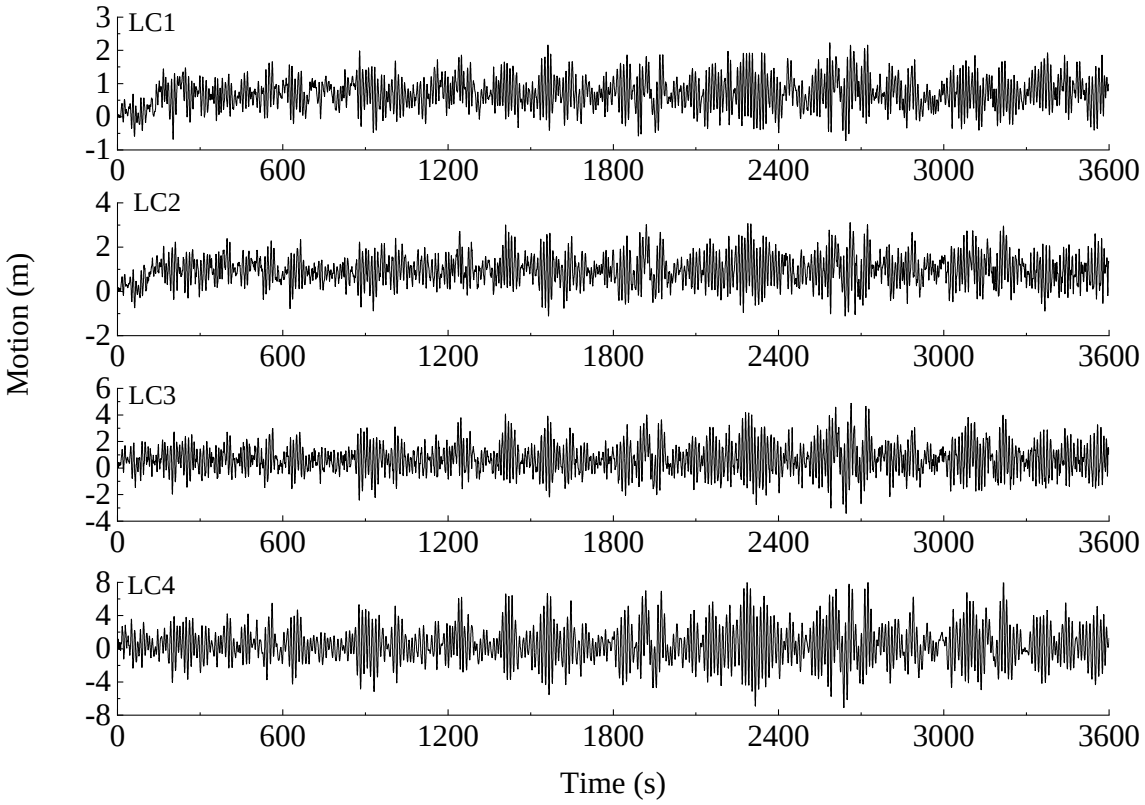

Figure 17 Time series of nacelle surge motion.

Table 9 Maximum nacelle acceleration

Load case	a_x (m/s^2)	a_y (m/s^2)	a_z (m/s^2)	$\sqrt{a_x^2 + a_y^2 + a_z^2}$ (m/s^2)
LC1	0.67	0.08	0.19	0.70
LC2	1.16	0.23	0.23	1.20
LC3	2.20	0.66	0.44	2.34
LC4	2.78	1.71	0.92	3.39

4.2.2.2 Inner pool surface elevation

The inner pool surface elevations, across the inner free water surface, are investigated in this subsection. Table 10 compares the wave elevations at the 5 reference points presented in Figure 18.

It is concluded that the inner free surface elevation across the inner pool is generally reduced compared to the free surface elevation outside the structure, although it is slightly amplified at Point 2 for load cases LC1 and LC2. The function of the vertical caisson as

breaking water is thus confirmed. Due to the shadow effect of the vertical caisson, the incident wave is suppressed when passing through the structure and thereby, the wave conditions in the pool are relatively calm. However, the movement of the platform induces radiation waves around the vertical caissons, explaining why the free surface elevation at Point 2 is amplified.

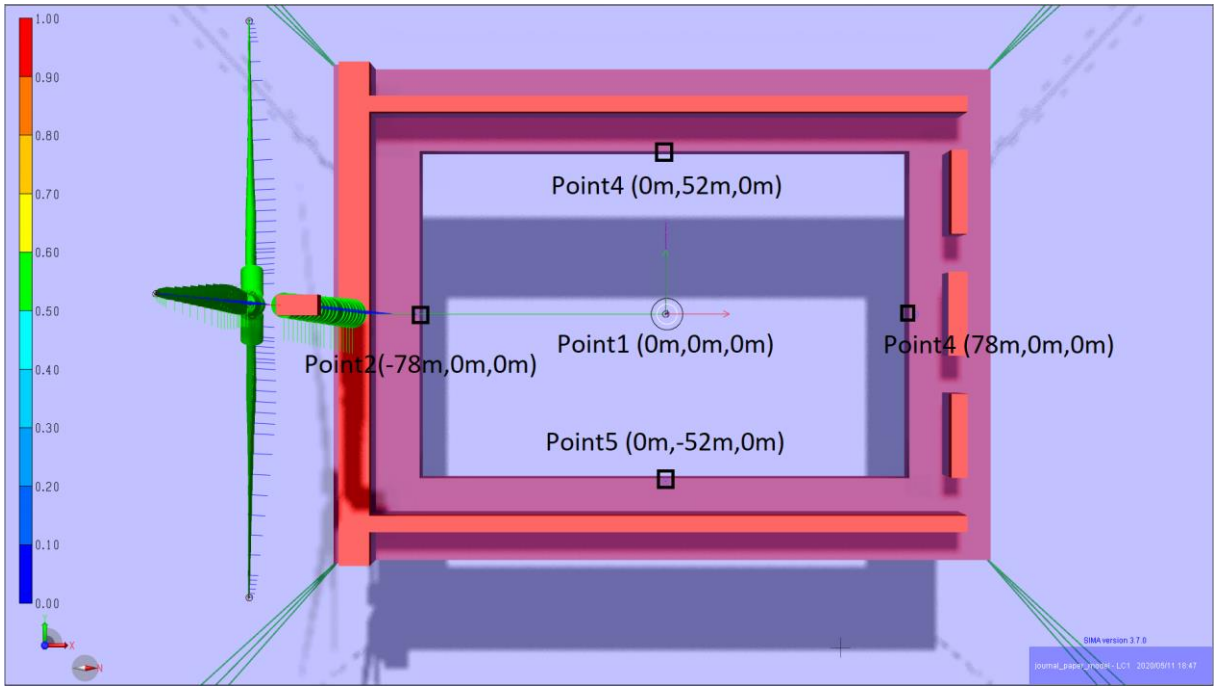

Figure 18 Reference points for inner free surface elevation.

Table 10 Standard deviation of wave elevation

Load case	Point1	Point2	Point3	Point4	Point5	Undisturbed wave
LC1	0.36 m	0.68 m	0.43 m	0.45 m	0.45 m	0.63 m
LC2	0.43 m	0.81 m	0.54 m	0.57 m	0.57 m	0.78 m
LC3	0.64 m	1.07 m	0.87 m	0.91 m	0.91 m	1.11 m
LC4	1.27 m	1.72 m	1.71 m	1.80 m	1.80 m	1.80 m

4.2.2.3 Tower base bending moment

As the flexible structural component that connects the wind turbine and the platform, the tower is subject to aerodynamic, hydrodynamic and inertial loads. It is one of the crucial interfaces dominating the structural integrity of the multi-purpose system. The tower base fore-aft bending moment is investigated in this section.

The mean value and standard deviation of tower base bending moment are plotted in Figure 19. The mean tower base bending moment is correlated to the wind speed. Within the below-rated wind speed range, the mean tower base bending moment increases with the wind speed, as expected. As the wind speed exceeds the rated value, the mean bending moment begins to drop due to the control strategy, which changes the blade pitch angle to reduce the aerodynamic load. In the survival state, the mean bending moment is approximately zero as the wind turbine is parked.

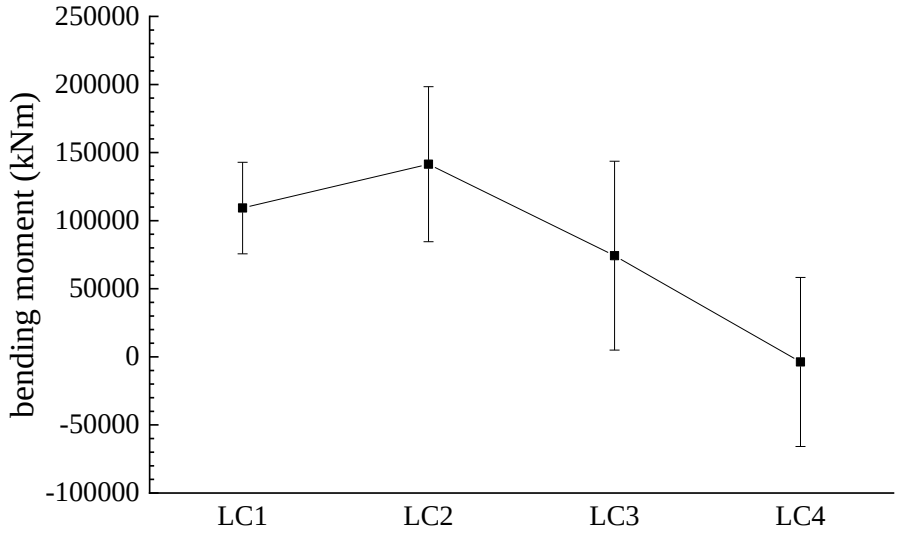

Figure 19 Mean value and standard deviation of tower base bending moment.

Generally, the standard deviation of tower base bending moment augments as the sea state becomes severe. Spectral analyses are performed to investigate further how the tower base responds to the aerodynamic and hydrodynamic excitations. Figure 20 shows the PSD of the tower base bending moment in rated and parked load cases. A multi-modal response is observed. One of response peaks is excited around wave frequency range as a result of the hydro-elastic coupling. Low frequency response is also observed. The thrust force varies slowly and thus induces low frequency bending moment oscillations in the tower base, which is a reflection of aero-elastic coupling. In addition, 1P frequency response is observed around 0.16 Hz. In the survival state, however, the low-frequency and 1P responses are dismissed as the blades have been pitched to feather in order to reduce the wind load. Figure 20 indicates that the aerodynamic load

can not be simplified as a quasi-static force in the assessment of structural response. Its dynamic effect is significant and thus must be addressed as a dynamic load.

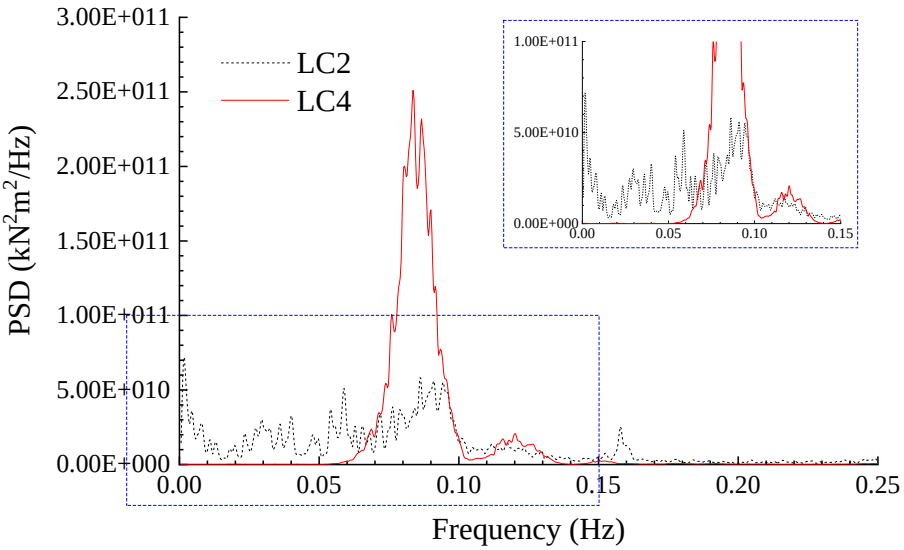

Figure 20 PSD of tower base bending moment.

Figure 21 shows the extrapolated up-crossing rate of tower base bending moment. It is identified that LC3 is the most critical load case whereas the tower base is less likely to exceed the ultimate limit state in LC4. The maxima of a random process is governed by both average value and oscillation range. Although the oscillation of bending moment is more significant in survival state due to stronger platform motions, the tower is subject to minimal wind turbine thrust force so that the average tower base bending moment is nearly zero. Therefore, the extreme bending moment is lower in the survival state (see Figure 22).

A further comparison of LC2 and LC3 shows that the bending moment is more likely to exceed a low-level threshold in the rated state. On the contrary, the up-crossing rate for high-level threshold is higher in the above-rated state. In the rated state, the thrust force acting on the rotor reaches its maximum so that the mean bending moment is larger. Therefore, the ultimate load has a higher probability of exceeding a low-level threshold. Comparatively, the bending moment oscillation is stronger in the above-rated state and thus the bending moment is more likely to exceed a high-level threshold. The same

interpretation applies to LC1 and LC4. It indicates that the aerodynamic load plays a significant role in the ultimate limit state of tower base.

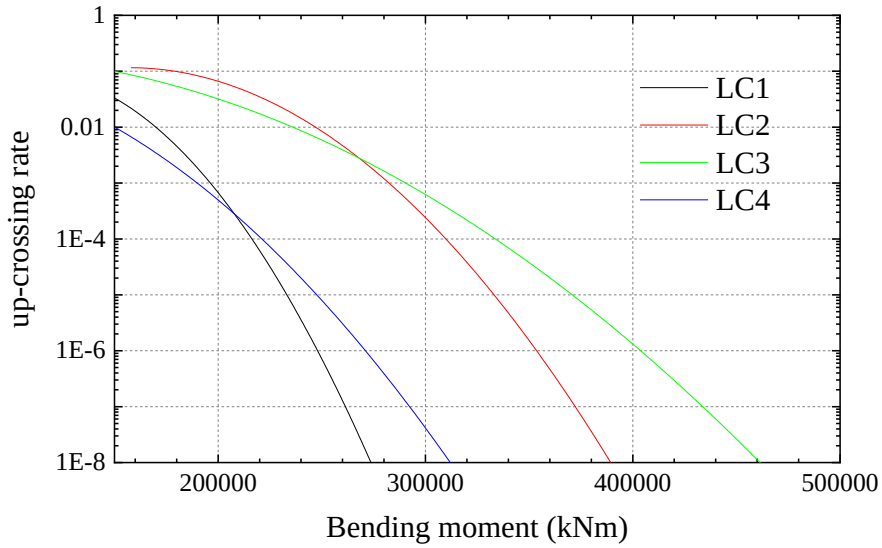

Figure 21 Extrapolated up-crossing rate of tower base bending moment.

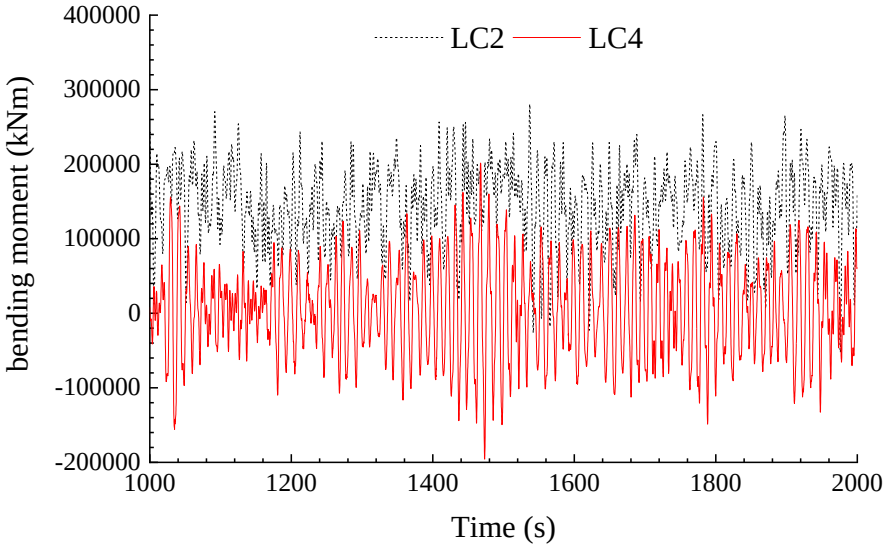

Figure 22 Time series of tower base bending moment.

4.2.2.4 Mooring line tension

The multi-purpose platform is moored through 12 catenary chain lines. Mooring line 5 is aligned with the wind and wave direction, so the tension force is the largest and thereby line 5 is investigated here. Figure 23 plots the tension force time series of the mooring line 5 in different load cases, and Figure 24 displays the associated up-crossing rate. The

analysis shows that the ultimate limit state of mooring line is dominated by wave load. Unlike what has been observed from tower base bending moment (Figure 21), The ultimate fairlead tension of line 5 purely increases with the significant wave height. In the survival state, where the significant wave height is H_s = 7.11 m, the largest ultimate mooring tension is observed. For example, the ultimate tension corresponding to 1e-4 is 1.23e4 kN, much larger than that of other load cases. Since the fairlead is attached to the platform, the mooring tension is totally governed by the platform motion. As presented in Section 4.2.2.1, the aerodynamic effect on platform motion is minor so that the mooring line tension is dominated by hydrodynamic load.

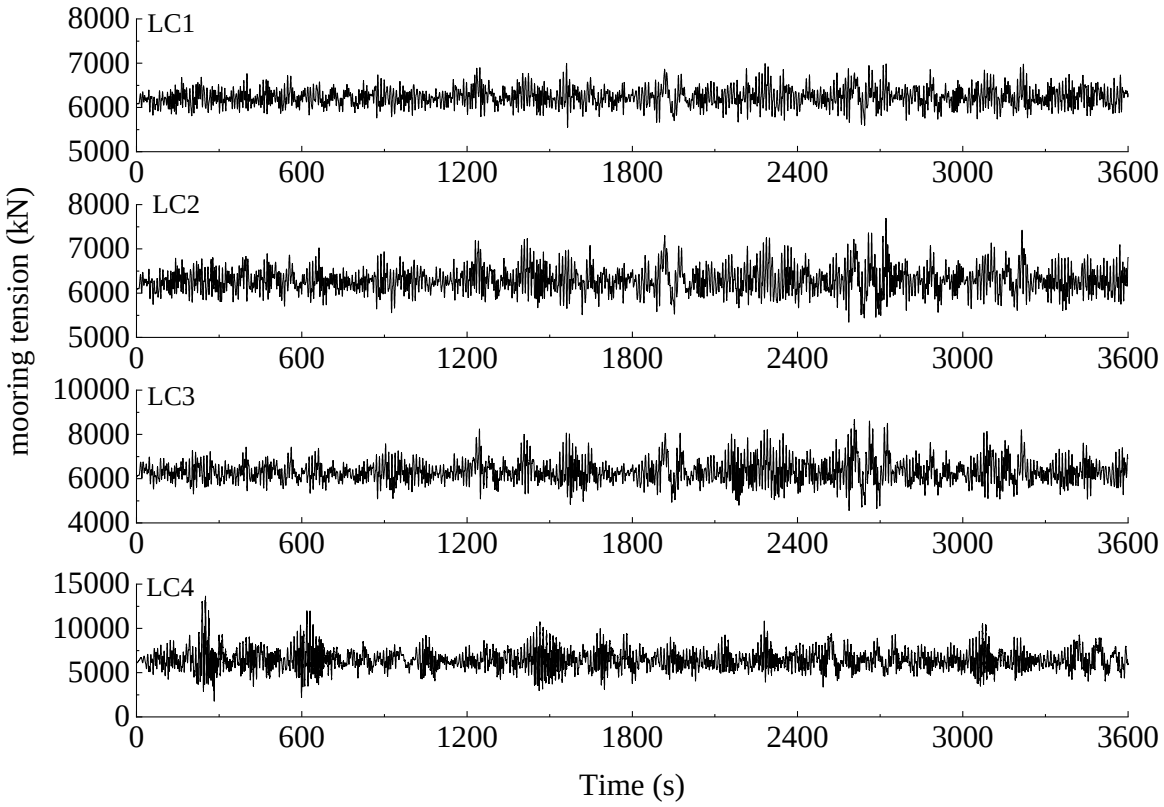

Figure 23 Time series of mooring line 5 tension force.

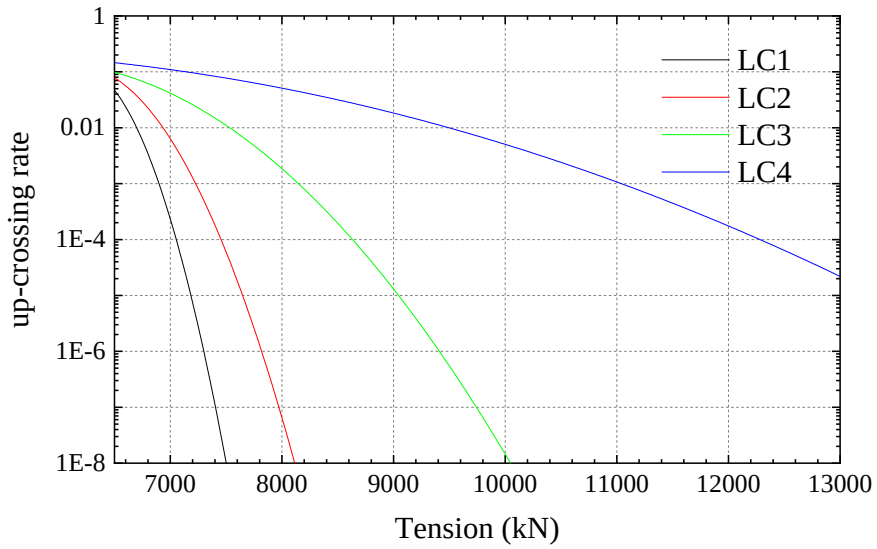

Figure 24 Extrapolated up-crossing rate of mooring line 5 tension force.

5 Conclusions

“The Blue Growth Farm” (Blue Growth Farm, 2019; Lagasco et al., 2019) is an H2020 project aimed at proposing a technological solution for the Blue Growth strategy proposed by the EU. Within this context, this work presents the numerical framework developed to support the conceptual design and analysis of the innovative multi-purpose platform configuration proposed by “The Blue Growth Farm” project.

For this purpose, a three-stage process has been adopted. Firstly, a numerically light, flexible, 2D strip theory-based parametric analysis has been carried out, in order to analyse a large design space and identify a suitable preliminary design for the section of the structure. Based on this parametric analysis, the cross section of the multi-purpose platform support structure is optimised to ensure that the natural periods of the system are outside typical 1st-order wave force period range – an objective fulfilled and confirmed by the later stage time-domain, fully coupled aero-hydro-servo-elastic analysis results.

Secondly, since the dimensions of the platform (Table 2) are relatively large, and the classic rigid body hypothesis for the support platform is questionable, a 3D hydro-elastic analysis of the support platform has been carried out. The results obtained show that no resonance phenomena are expected between the input loads (including those from wind turbine) and the structure rigid and flexible natural frequencies. Further, they demonstrate

that the first six modes, i.e. those related to the rigid body motions of the structure, cumulatively interest more than 99.99% of the mass participation ratios in all the directions, i.e. the coupled dynamic analyses can be performed considering the support platform as a rigid body, and modelling as flexible elements only the tower and the blades of the wind turbine.

Finally, a nonlinear, fully coupled model of the whole multi-purpose platform is developed and applied to derive the dynamic responses of this platform, considering four load cases, and proposing a novel approach to linearise the effect of the wave energy converters on the global motion. It should be noted that strong nonlinear hydrodynamic phenomena, like slamming and green water, are beyond the capabilities of the adopted approach. These limitations suggest that further more accurate analyses could be necessary in advanced design phases. As primary key performance indicators, the platform global rigid body motion, the nacelle acceleration, the tower base bending moment, and the mooring line tension forces have been investigated. A modified up-crossing rate method has been employed to assess the ultimate limit states of tower base and mooring line.

With reference to the particular case study presented, the technical feasibility of the BGF multi-purpose platform design proposed is confirmed and an optimized support platform shape is found. This is a fundamental achievement and paves the way to further studies on the innovative concept proposed. Also, the impact of the floating support structure elasticity is proved to be negligible for the assessment of the overall coupled dynamics. This result represents an advance to the state-of-art relative to large floating structures and may be useful also for studies of similar structures in the future.

Acknowledgements

This work has been produced in the framework of the Blue Growth Farm project (http://www.thebluegrowthfarm.eu/), which has received funding from the European Union's Horizon 2020 research and innovation programme under Grant Agreement number 774426. The content of the work does not report the opinion of the European Commission and reflects only the views of the author(s), including errors or omissions.

The European Commission is also not liable for any use that may be made of the information contained herein.

The first author also acknowledges the financial support of State Key Laboratory of Hydraulic Engineering Simulation and Safety, Tianjin University (Grant No. HESS-1919).

References

ANSYS. https://www.ansys.com/. [accessed 14 February 2020]

Ansys Aqwa. https://www.ansys.com/products/structures/ansys-aqwa. [accessed 14 February 2020]

Aubault, A., Alves, M., Sarmento, A., Roddier, D., Peiffer, A., 2011. Modeling of an oscillating water column on the floating foundation WindFloat, ASME 2011 30th International Conference on Ocean, Offshore and Arctic Engineering. American Society of Mechanical Engineers, pp. 235-246.

Bachynski, E.E., 2018. Fixed and Floating Offshore Wind Turbine Support Structures, Offshore Wind Energy Technology. Wiley.

Bachynski, E.E., Moan, T., 2013. Point absorber design for a combined wind and wave energy converter on a tension-leg support structure, ASME 2013 32nd International Conference on Ocean, Offshore and Arctic Engineering. American Society of Mechanical Engineers.

Bard, J., 2014. Multi-use Platform Concepts for the Oceans of Tomorrow, International Conference Ocean Energy, Halifax, Nova Scotia Canada.

Blue Growth Farm. https://cordis.europa.eu/project/id/774426. [accessed 14 February 2020]

Boccotti, P., 2002. Caisson for absorbing wave energy. US Patents.

Bak C., Zahle F., Ritsche, B., Kim, T., Y, A., Henriksen, L.C., Natarajan, A., Hansen, M.H., 2013. Description of the DTU 10 MW Reference Wind Turbine.

Coulling, A.J., Goupee, A.J., Robertson, A.N., Jonkman, J.M., 2013. Importance of second-order difference-frequency wave-diffraction forces in the validation of a FAST semi-submersible floating wind turbine model, ASME 2013 32nd International Conference on Ocean, Offshore and Arctic Engineering. American Society of Mechanical Engineers.

Cummins, W., 1962. The impulse response function and ship motions. David Taylor Model Basin, Washington DC, pp. 101-109.

Dalton, G., Bardocz, T., Blanch, M., Campbell, D., Johnson, K., Lawrence, G., Lilas, T., Friis-Madsen, E., Neumann, F., Nikitas, N., Ortega, S.T., Pletsas, D., Simal, P.D., Sorensen, H.C., Stefanakou, A., Masters, I., 2019. Feasibility of investment in Blue

Growth multiple-use of space and multi-use platform projects; results of a novel assessment approach and case studies. Renewable & Sustainable Energy Reviews 107, 338-359.

DNV, 1994. WADAM—Wave Analysis by Diffraction and Morison Theory, SESAM user's manual, Høvik.

DNV GL, 2017. DNVGL-RP-C205, Recommended Practice–Environmental Conditions and Environmental Loads.

European Commission, 2012. Blue Growth - opportunities for marine and maritime sustainable growth (Brussels, 13.9.2012 COM(2012) 494 final).

European Commission, 2011. Scenarios and drivers for Sustainable Growth from the Oceans. Seas and Coasts, First Interim Report, ECORYS for EC, DG MARE, Rotterdam/Brussels.

European Commission, Blue Growth, 2018
https://ec.europa.eu/maritimeaffairs/policy/blue_growth. [accessed 14 February 2020]

H2Ocean, 2012, http://www.h2ocean-project.eu/. [accessed 14 February 2020]

Hansen, M.O., 2015. Aerodynamics of wind turbines. Routledge.

Johannessen, K., Meling, T.S., Hayer, S., 2001. Joint distribution for wind and waves in the northern north sea, The Eleventh International Offshore and Polar Engineering Conference. International Society of Offshore and Polar Engineers.

Lagasco, F., Vassalli, F., Pennino, R., Gentile, G., Fiacco, L., G. Urbano, P., 2019. New engineering approach for the development and demonstration of a multi-purpose platform for the blue growth economy, 38th International Conference on Ocean, Offshore and Arctic Engineering, Glasgow, UK.

Lamas-Pardo, M., Iglesias, G., Carral, L., 2015. A review of Very Large Floating Structures (VLFS) for coastal and offshore uses. Ocean Engineering 109, 677-690.

Li, L., Cheng, Z.S., Yuan, Z.M., Gao, Y., 2018a. Short-term extreme response and fatigue damage of an integrated offshore renewable energy system. Renewable Energy 126, 617-629.

Li, L., Collu, M., Ruzzo, C., Failla, G., Abhinav, K.A., Arena, F., 2019a. Analysis of the coupled dynamics of an offshore floating multi-purpose platform, Part A: rigid body analysis, 38th International Conference on Ocean, Offshore and Arctic Engineering, Glasgow, Scotland.

Li, L., Gao, Y., Hu, Z.Q., Yuan, Z.M., Day, S., Li, H.R., 2018b. Model test research of a semisubmersible floating wind turbine with an improved deficient thrust force correction approach. Renewable Energy 119, 95-105.

Li, L., Gao, Y., Yuan, Z.M., Day, S., Hu, Z.Q., 2018c. Dynamic response and power production of a floating integrated wind, wave and tidal energy system. Renewable Energy 116, 412-422.

Li, L., Yuan, Z.M., Gao, Y., Zhang, X.S., Tezdogan, T., 2019b. Investigation on long-term extreme response of an integrated offshore renewable energy device with a modified environmental contour method. Renewable Energy 132, 33-42.

Malara, G., Romolo, A., Fiamma, V., Arena, F., 2017. On the modelling of water column oscillations in U-OWC energy harvesters. Renewable Energy 101, 964-972.

Mavrakos, S.A., 2004. Hydrodynamic coefficients in heave of two concentric surface-piercing truncated circular cylinders. Applied Ocean Research 26(3-4), 84-97.

MERMAID, 2014. http://www.vliz.be/projects/mermaidproject/index.html. [accessed 14 Feburary 2020]

Michailides, C., Luan, C., Gao, Z., Moan, T., 2014. Effect of flap type wave energy converters on the response of a semi-submersible wind turbine in operational conditions, ASME 2014 33rd International Conference on Ocean, Offshore and Arctic Engineering. American Society of Mechanical Engineers.

Molin, B., Remy, F., Camhi, A., Ledoux, A., 2009. Experimental and numerical study of the gap resonances in-between two rectangular barges, 13th congress of international maritime association of mediterranean, Instanbul, Turkey.

Molin, B., Zhang, X., Huang, H., Remy, F., 2018, On natural modes in moonpools and gaps in finite depth. Journal of Fluid Mechanics, 840: 530-554.

Muliawan, M.J., Karimirad, M., Moan, T., 2013. Dynamic response and power performance of a combined spar-type floating wind turbine and coaxial floating wave energy converter. Renewable Energy 50, 47-57.

Naess, A., Gaidai, O., 2009. Estimation of extreme values from sampled time series. Structural Safety 31(4), 325-33.

Pachauri, R.K., Allen, M.R., Barros, V.R., 2014. Climate change 2014: synthesis report. Contribution of Working Groups I, II and III to the fifth assessment report of the Intergovernmental Panel on Climate Change. IPCC; 2014.

Ruzzo, C., Failla, G., Arena, F., M.Collu, Li, L., Mariotti, A., 2019. Analysis of the coupled dynamics of an offshore floating multi-purpose platform, Part B: hydro-elastic analysis with flexible support platform, 38th International Conference on Ocean, Offshore and Arctic Engineering, Glasgow, Scotland.

SINTEF Ocean, 2019a. RIFLEX Theory Manual.

SINTEF Ocean, 2019b. SIMO Theory Manual.

Øye, S., 1991. Dynamic stall simulated as time lag of separation, Proceedings of the 4th IEA Symposium on the aerodynamics of wind turbines.

Tony Burton, David Sharpe, Nick Jenkins, Bossanyi, E., 2001. Wind Energy Handbook. John Wiley & Sons, Ltd.

Tropos, 2012. http://www.troposplatform.eu/. [accessed 14 February 2020]

Wang, C.M., Tay, Z.Y., 2011. Very Large Floating Structures: Applications, Research and Development. Proceedings of the Twelfth East Asia-Pacific Conference on Structural Engineering and Construction (Easec12) 14.

Wei, W., Fu, S.X., Moan, T., Song, C.H., Ren, T.X., 2018. A time-domain method for hydroelasticity of very large floating structures in inhomogeneous sea conditions. Marine Structures 57, 180-192.

Wolgamot, H.A., Taylor, R.E., Taylor. P.H., 2015. Radiation, trapping and near-trapping in arrays of floating truncated cylinders. Journal of Engineering Mathematics, 91:17–35.